Chapter 15
Surface Generation Process with Consideration of the Balancing State in Diamond Machining

C. Brandt, A. Krause, J. Niebsch, J. Vehmeyer, E. Brinksmeier,
P. Maass, and R. Ramlau

Abstract. In order to manufacture optical components or mechanical parts with high requirements regarding surface quality, diamond machining is frequently applied. Nevertheless, to achieve the desired surface quality, the understanding of the surface generation process and its influencing parameters is highly important. One crucial parameter is the residual unbalance of the main spindle. As the residual unbalance affects the process and vice versa, the investigation of the process-machine interaction is necessary. In this paper results of experimental work and mathematical modelling of diamond machining under varying balancing states are presented. The experiments show the connection between unbalances and resulting surface quality; the mathematical model provides the possibility to simulate the surface quality for given unbalances distributions. Furthermore, regularization techniques in order to solve the inverse problem of computing the optimal balancing state for a given or desired surface quality are presented.

15.1 Introduction

Ultraprecision diamond machining is mainly used to manufacture optical parts or microstructures with form deviations of less then one micron and surface roughness in the range of a few nanometers. To obtain these accuracies the requirements regarding machine tool accuracy, process control and environmental conditions are exceptional.

But even if all these requirements are met, unintended vibrations either induced by the environment or by the process itself can result in insufficient part quality. Usually external vibrations can be kept low by appropriate foundations of the machine tool. In contrast, process induced vibrations can occur because of misaligned tools or workpieces, unsymmetrical workpieces, unsymmetrical workpiece mounting or inhomogeneous workpiece materials. All these effects lead to non-homogeneous mass distribution for the rotational axis of the system and therefore to vibrations when under rotation. If existent these process induced vibrations can lead to an

B. Denkena and F. Hollmann (Eds.): Process Machine Interactions, LNPE, pp. 329–360.
springerlink.com

increased form deviation and an increased surface roughness depending on the exciting frequency. Therefore, precision balancing is crucial for ultraprecision machining processes [7]. In this chapter only ultraprecision turning will be considered, nevertheless basic balancing principles will apply for other processes using rotating spindles as well. The balancing process in ultraprecision machining is done manually and it generally takes more than one iteration step to get the best balancing condition.

The goal of the project is to get a deeper understanding of the interaction between balancing and the surface generation process in ultraprecision machining. Therefore, a process-machine model has been developed which allows to predict the surface topography based on the balancing state considering the interaction between the machine tool structure and the machining process. In a first step, we developed an interaction model for the experimental platform, see Section 15.3. A structure model was developed to determine the vibrations for given force and moment distributions induced by unbalances as well as forces from the cutting process. This model can also be utilized to determine unbalance distributions or balancing weights from vibration data measured by sensors during idle spindle speed. Additionally, an analytical process model for describing the cutting forces during the cutting process has been developed. The cutting forces were related to the surface structure of the workpiece. Since the cutting forces influence the vibrations of the machine and vice versa, both sub-models have to be merged into a mechanical-dynamical model. The complete model will enable us to determine the effective cutting forces and displacements related to the workpiece surface. This model also allows to compute the surface quality and in the future a necessary balancing state to achieve a needed surface quality.

15.2 Balancing in Ultraprecision Diamond Machining

Balancing procedures are commonly used wherever rotating parts or spindles (referred to as rotors) are not allowed to exceed a certain eccentricity. To specify a balanced or unbalanced rigid rotor respectively, the balance quality grade G is used. The balance quality grade represents the tolerable track speed (mm/s) of the center of gravity: $G = e_{zul}\omega$ where e_{zul} is the tolerable eccentricity and ω the angular velocity. For example $G6.3$ stands for a tolerable track speed of 6.3 mm/s. Within the DIN ISO 1940-1 quality grades from $G6.3$ down to $G0.4$ are considered for conventional machining [1]. These values are summarized in a diagram (Fig. 15.1). The diagram allows for instance to obtain a tolerable specific unbalance for a needed G value and the operating speed n. Additionally, these G values are standardized for characteristic machine tool constructions where the mass of the rotor is within a defined range of the total mass [13]. To show the difference between balancing in conventional machining and ultraprecision machining the diagram has been extended by the G value range which was set as a target for the project described in this article. The named target range for ultraprecision machining is $G0.04$ or less (depicted area, Fig. 15.1).

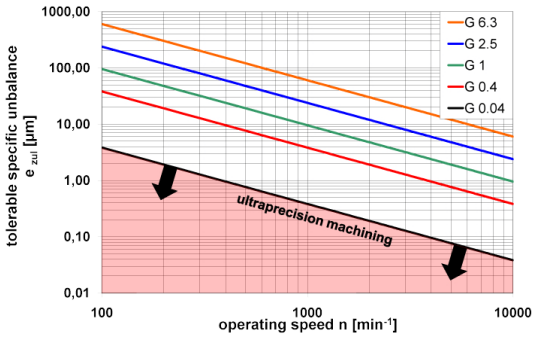

Fig. 15.1 Balance quality grades

15.2.1 Single-Plane Balancing

For ultraprecision machine tools rigid rotor behavior can be assumed for the main spindle, which means the rotor will not or only insignificantly change its form or unbalance state while running with operational speed or slower. In principle every unbalance state for a rigid rotor can be compensated with two balancing planes [13, 18]. In general these unbalances can be classified into three different types: static unbalance, moment unbalance and dynamic unbalances.

A static unbalance occurs when a single unbalance is set to the radial plane of a fully balanced rotor (Fig. 15.2). Hence, the center of gravity will be shifted away from the shaft axis. When the spindle starts to rotate the unbalance will cause a centrifugal force and therefore a vibration of the system. This kind of unbalance can be compensated by either removing material from the spindle in the direction of the unbalance or by adding a counterweight in the opposite direction of the unbalance. The unbalance can be detected without continuous rotation of the spindle. The compensation procedure is called single-plane-balancing (static balancing), because the compensation is done in a single plane only [13]. Strictly speaking the above example is only valid for a two dimensional system. But, although all real systems are three dimensional, some may be treated as two dimensional [4].

A moment unbalance is caused by two identical unbalances, regarding their absolute value, which are located opposite to each other in different radial planes (Fig. 15.3). This unbalance cannot be detected without rotating the spindle. Under rotation the two occurring unbalances will cause opposing centrifugal forces in different planes and therefore a moment to the spindle will occur [13]. The described

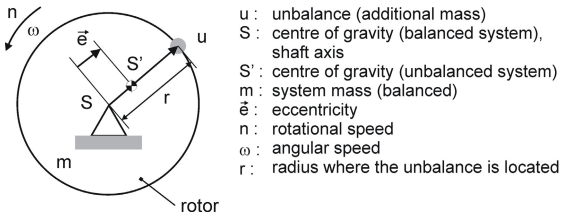

Fig. 15.2 Static unbalance of a planar rotor [5]

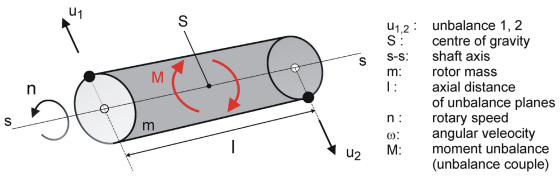

Fig. 15.3 Moment unbalance [5]

effect will be referred to as moment unbalance. As well as a static unbalance, a moment unbalance is mainly theoretical or will be used to describe a rotor or spindle where the main influence is given by the moment unbalance. The depicted two kinds of unbalances are necessary to describe and understand unbalances which occur in real spindle systems. These unbalances are called dynamic unbalance and can be described as a combination between a static unbalance and a moment unbalance. Fig. 15.4 shows an example of dynamic unbalance. The center of gravity for the workpiece and the counter weight could not be aligned within the balancing plane. Therefore, the overlapping workpiece lead to a moment unbalance for the rotating spindle.

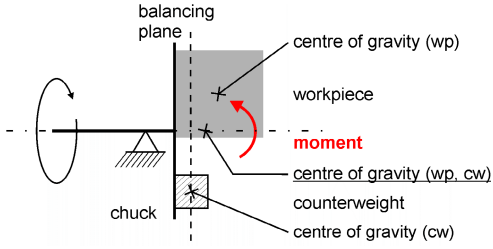

Fig. 15.4 Dynamic unbalance with single-plane balancing (static balancing) [4]

15.2.2 Dual-Plane Balancing

The described process of single-plane balancing is only capable of compensating static unbalances. Furthermore, for most balancing setups a moment will be induced because of the axial distance between balancing plane and unbalance. The general balancing condition for most workpieces is called dynamic unbalance. It can be regarded as a combination between static unbalance and a moment unbalance.

This dynamic unbalance can be compensated with a second balancing plane within which a compensatory moment can be applied, see Fig. 15.5. With two balancing planes it is possible to compensate for all unbalance situations that may occur, as long as the spindle can be considered as rigid [13]. Nevertheless, a second balancing plane is increasing the complexity of the system and therefore, the effort to balance a system will be increased too.

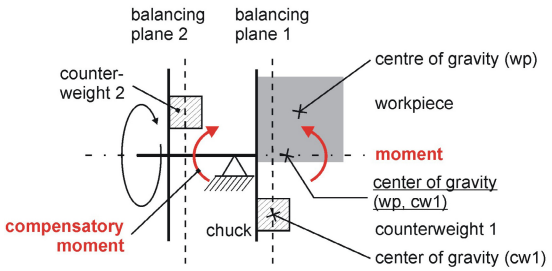

Fig. 15.5 Dual-plane-balancing principle [4]

15.2.3 Ultraprecision Machine Tools

For most ultraprecision machine tools balancing is a manual, iterative and time consuming process with the goal to minimize the occurring vibrations. This process has to be carried out whenever the workpiece is changed, because a small difference in position can lead to a significant unbalance. Depending on workpiece size and mounting situation (centric or eccentric), a rough balancing is done by applying a counter weight. The fine balancing is done by applying set screws to the chuck.

15.2.4 Balancing Dependent Surface Generation

Because of the high requirements for the machined surfaces in ultraprecision machining it is necessary to understand to which extent the surface generation process is influenced by the different process parameters. For this chapter the surface generation will be observed and investigated with regard to the balancing state of the main spindle. As mentioned before balancing is one crucial factor for ultraprecision machining but up to now it has not been investigated to which magnitude an occurring unbalance influences the surface topography or the surface generation process respectively.

To characterize the surface topography of the generated surfaces different measurement devices are used. The form is measured by using an optical flatness tester, where it is possible to assess the whole surface of the chosen samples. Roughness measurements are taken by white light interferometry and by tactile profilometry (s. Chap 1, Sect. 4 Workpiece analysis).

15.2.5 Process Forces with Regard to Unbalances

During machining an unbalance will lead to a deflected workpiece and therefore change the depth of cut and consequently the process forces periodically. As the process forces also act on the tool, the tool will be deflected as well. It can be estimated, that the cutting force will deflect the tool opposite to the cutting direction, but the tool will also be moved away from the surface and therefore reduce the effective depth of cut. In consequence, the cutting force will be reduced and the tool

will move back in cutting direction and towards the surface as well. Depending on the occurring forces, the damping properties of the tool and the unbalance, the tool will either start to vibrate itself or it will reach a state of equilibrium.

Due to the interaction between the workpiece and the tool the surface of the workpiece will be distorted. For an unbalanced and therefore vibrating workpiece the engaged tool will act as a damper and reduce the induced vibrations. Due to this process machine interaction it is necessary to take the process forces into account with regard to the unbalance state and the resulting surface topography . But, because of size effects process models applied in conventional machining cannot be applied. Previous investigations showed that in diamond turning the forces increase for higher cutting velocities [11] whereas in conventional machining the forces decrease at higher cutting velocities because of heating and softening of the workpiece material [14].

To assess the process forces during ultraprecision machining measurements have been carried out using a triaxial dynamometer for low forces. The dynamometer is mounted beneath the tool holder, on top of the test stands z-axis.

15.3 Experimental Setup

Commercially available ultraprecision machine tools are designed for manual single-plane balancing and therefore, it is not possible to compensate for dynamic unbalances. But, if a second balancing plane would be applied to an ultraprecision machine tool a rise in workpiece quality relating to surface roughness and form accuracy can be assumed.

To investigate the influence of dual-plane balancing in ultraprecision diamond machining a test stand has been designed and built. Balancing experiments have been carried out to investigate the influence between surface topography and corresponding balancing situation. As the main goal of the investigations is to identify and characterize balancing dependent effects during ultraprecision machining the experimental procedure has been kept as simple as possible to reduce the influence of other effects. For this reason face turning was chosen as machining process and plane discs (Fig. 15.6) were machined. As a result only one axis has to be moved during machining. For all experiments an aluminum alloy (AlMg3) was used a workpiece material which is commonly used for ultraprecision machining processes.

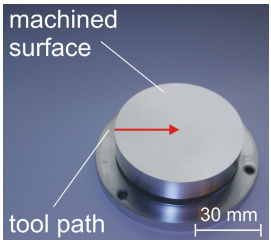

Fig. 15.6 Machined planar sample

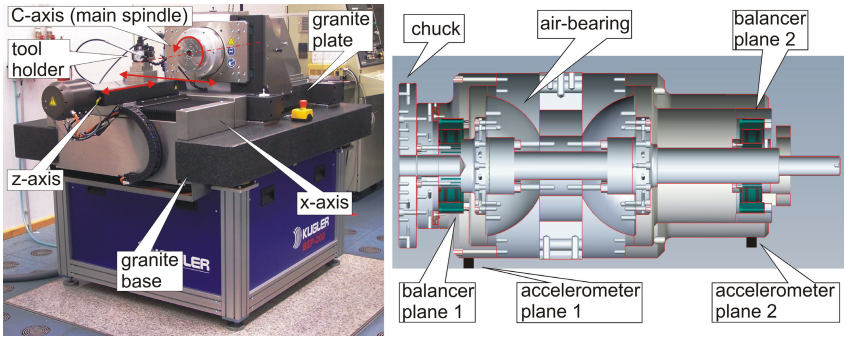

Fig. 15.7 Balancing experiment platform (test stand), cross sectional view of the main spindle (courtesy: Kugler) [5]

15.3.1 Test Stand

The test stand (Fig. 15.7, left) is based on an ultraprecision turning lathe, which contains an automatic dual-plane balancing system. This system consists of two independent balancing actuators, so called balancers, both attached to the spindle. The first balancer is located in front of the air bearing near the chuck, the second is located behind the air bearing near the motor (Fig. 15.7, right). Attached to the spindle housing are two vibration sensors located in same radial plane as the corresponding balancers. Their signal is send to a control unit for analyzing and interpreting the vibration data. The control unit calculates a balancing solution according to the analyzed vibration data and sends a control impulse to each balancer. Because each adjustment that is made to a balancer is simultaneously influencing both balancing planes, the control unit is not able to calculate a single step solution, but has to approximate iteratively the best solution. This procedure demonstrates the complexity of dual-plane balancing. For the functional principle of a single balancer and the customizable machine tool properties, see [4, 5, 6].

15.4 Structure Process Interaction Model

In order to improve the balancing process with mathematical methods, a simulation environment of the whole process has to be developed. The crucial point hereby is the connection between unbalances and surface topography. Therefore, a model which considers the interaction between machine structure and cutting process has been built up. In the following subsections the separate parts of this model are presented, namely the machine model in 15.4.1, the process model in 15.4.2, the coupling in 15.4.3 and the visualization of the surface topography in 15.4.4.

15.4.1 The Structure Model

The experimental platform from Fig. 15.7 has a complex structure which is difficult to model in full detail. Thus, simplifying assumptions have been made that enable us to handle the model mathematically but also make sure that the simplified model is still a good approximation of the reality.

15.4.1.1 System Matrices

First, we have divided the platform into components which are illustrated in Fig. 15.8, namely the rotating part of the spindle, the spindle casing, the rotating part of the motor, and the motor casing. The spindle rotor and casing are connected by an air bearing with two spherical calottes. We have modelled this bearing by two spring-damper elements although in a first attempt any damping in the springs was neglected. The motor bearings are also modelled as spring-damper elements. Spindle and motor are connected by a coupling that can compensate misalignments in axial and radial directions as well as torsion. It is also modelled as a spring element. Spindle and motor are supported by a granite base that is assumed to be rigid. The joints to the granite base are modelled as firm spring elements. Additionally, Figure 15.8 shows the coordinate system. In operation, the spindle rotates counterclockwise around the z-axis.

Secondly, we have developed a vibration model for each part of the machine separately. If we would consider only unbalances as possible reasons for vibrations it would be sufficient to allow vibrations in radial directions x and y only. Since unbalances cause harmonic vibrations and we assume isotropic bearings, the vibrations in x and y direction are the same except for a phase shift of $\pi/2$. Nevertheless, the forces from the cutting process act in all three directions. Thus each point along the z-axis, i.e. each beam element of infinitesimal length ∂z, has the following degrees of freedom (DOF): the displacement u, v, w in x, y, z direction, the torsion angle β_z, and the rotational angles β_x, β_y. We collect the DOF in a vector $u = u(z,t)$. The computation of u is based on an energy formulation, the so called Principle of Virtual Displacements, see [8], Chapter 5. This principle is equivalent to equilibrium conditions from which a partial differential equation for $u(x,t)$ can be derived. Starting from the energy formulation, we use the Finite Element Method (FEM) for the discretization in the space variable x. We arrive at a system of ordinary differential equations (ODE) in time of the form

$$\mathbf{M}\ddot{\mathbf{u}}(t) + \mathbf{S}\mathbf{u}(t) = \mathbf{p}(t), \tag{15.1}$$

where $\mathbf{M}$ denotes the mass matrix, and $\mathbf{S}$ the stiffness matrix. In case of damping in the system a third term $\mathbf{D}\dot{\mathbf{u}}(t)$ on the left hand side with a sparse damping matrix $\mathbf{D}$ would be added. For the discretization, the considered parts of the platform are divided into elements with nodes at each end. The movement of each point between the nodes is described by ansatz functions scaled with the movement of the nodes. Considering the boundary and transition conditions between the end node of one element and the first node of the next element we will get system matrices $\mathbf{M}$ and

S for each part of the platform. This procedure is well known and we have mainly followed [8] in order to derive the matrices. We have used the following partition:

1. Spindle rotor with the coupling: 36 elements.
2. Spindle casing: 30 elements.
3. Rotor part of the motor: 3 elements.
4. Motor casing: 2 elements.

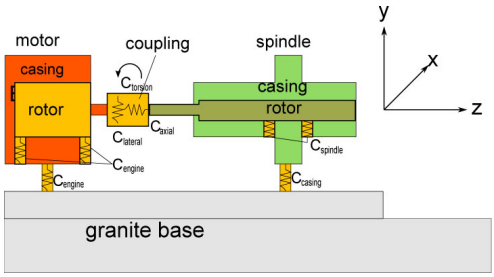

Fig. 15.8 Modeled parts of the test stand

As introduced above, each node has 6 degrees of freedom (DOF). The DOF of each of the parts specified above are collected in vectors $\mathbf{u}_{sp-rot}, \mathbf{u}_{sp-cas}, \mathbf{u}_{m-rot}, \mathbf{u}_{m-cas}$. A discretization in N_i elements in our model leads to $N_i + 1$ nodes and thus $6 \cdot (N_i + 1)$ DOF in the model of the ith part. The vectors of DOF are subject to equation (15.1) with mass matrices $\mathbf{M}_{sp-rot}, \mathbf{M}_{sp-cas}, \mathbf{M}_{m-rot}, \mathbf{M}_{m-cas}$ and stiffness matrices $\mathbf{S}_{sp-rot}$, $\mathbf{S}_{sp-cas}$, $\mathbf{S}_{m-rot}$, $\mathbf{S}_{m-cas}$. If we collect all DOF in one vector

$$\mathbf{u} = (\mathbf{u}_{sp-rot}^T, \mathbf{u}_{sp-cas}^T, \mathbf{u}_{m-rot}^T, \mathbf{u}_{m-cas}^T)^T, \tag{15.2}$$

we get a block diagonal structure for the entire mass and stiffness matrix of the dimension 450×450.

Additionally, we have to consider the bearing elements that connect the DOF of the corresponding nodes in the connected parts via a stiffness parameter C and damping parameters D. This results in additional diagonal and in off-diagonal elements of the entire stiffness matrix which are collected in sparse matrices $\mathbf{C}_{air}$ for the air bearing, $\mathbf{C}_m$ for the motor, and $\mathbf{C}_c$ for the coupling of motor and spindle:

$$\mathbf{S} = \begin{pmatrix} \mathbf{S}_{sp-rot} & \mathbf{0} & \mathbf{0} & \mathbf{0} \\ \mathbf{0} & \mathbf{S}_{sp-cas} & \mathbf{0} & \mathbf{0} \\ \mathbf{0} & \mathbf{0} & \mathbf{S}_{m-rot} & \mathbf{0} \\ \mathbf{0} & \mathbf{0} & \mathbf{0} & \mathbf{S}_{m-cas} \end{pmatrix} + \begin{pmatrix} \mathbf{C}_{air} & -\mathbf{C}_{air} & \mathbf{0} & \mathbf{0} \\ -\mathbf{C}_{air} & \mathbf{C}_{air} + \mathbf{C}_c & -\mathbf{C}_c & \mathbf{0} \\ \mathbf{0} & -\mathbf{C}_c & \mathbf{C}_c + \mathbf{C}_m & -\mathbf{C}_m \\ \mathbf{0} & \mathbf{0} & -\mathbf{C}_m & \mathbf{C}_m \end{pmatrix}. \tag{15.3}$$

The damping matrix **D** will have the same structure as the additional sparse matrices in the stiffness matrix. Stiffness values for the coupling between motor and spindle were provided by the manufacturer. For the air bearing between spindle and spindle casing we had to rely on an inspection record that stated measurement

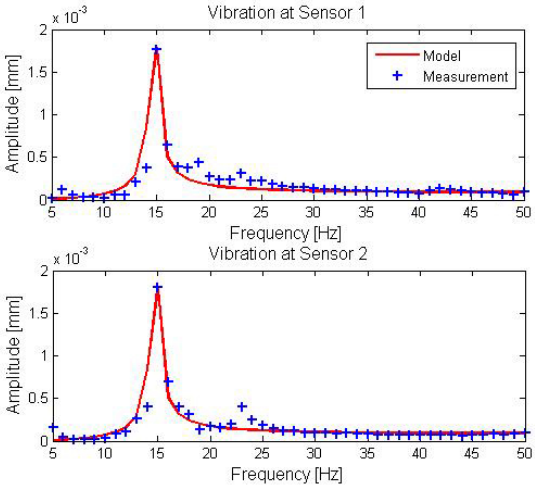

Fig. 15.9 Comparison of model and measurement data for given unbalance. The two sensors are fixed in y-direction on the casing above the two balancers [2]

values for the axial and radial stiffness of the bearing in the steady state. We mention again, that we have neglected the damping in a first attempt mainly because of the lack of information. The identification of damping coefficients will be part of future investigations.

15.4.1.2 Model Adjustment

Although we have carefully modelled the elements with respect to their geometry and physical properties, we still made simplifications. Therefore, the model may not fit reality immediately. The most uncertain values are the stiffness parameters for the bearings, in particular those from the air bearing. A modal analysis of the experimental platform was carried out in order to adjust the model eigenfrequencies to the eigenfrequencies of the platform but the analysis turned out to be faulty. So far, the only reliable information we have of the real platform are the vibrational data for certain defined unbalance settings in a frequency range of $5 \cdots 50$ Hz. For a good model, the measured data has to fit the computed data reasonably well. With the pre-chosen model parameters we were not able to achieve this data fit immediately. Hence, we have changed the stiffnesses for all bearings and monitored its effect on the vibrational response. It turned out that the stiffness of the air bearing changed the vibrational behavior most notably, i.e. a reduction of its stiffness produced a desired eigenfrequency at 15 Hz. The influence of other bearings on the lower eigenfrequencies was insignificant. A comparison of the data produced by the model with the measurements can be seen in Fig. 15.9. Although this first attempt to optimize the model according to the sparse information was successful, it is still questionable if the model reflects the machine correctly in all necessary aspects. It is planned to carry out further modal analyses in the near future. With these data available, a more reliable model can be generated. Meanwhile, we have used this model for further computations and tests, in particular the combination with the force model.

15.4.1.3 Solution of the Vibration Equation in the Presence of Unbalances

If only unbalances in our machine tool are considered, the right hand side $\mathbf{p} = \mathbf{p}_{unb}(t)$ of equation (15.1) has harmonic entries depending on the angular velocity ω. In practice, the revolution speed n in rpm is given, therefore we have $\omega = \frac{2\pi}{60}n$. An unbalance is modelled as a mass Δm displaced from the shaft by a vector $\mathbf{r} = re^{i\cdot\phi}$ where ϕ is the angle to a given zero position. If the displaced mass rotates with an angular velocity ω it induces a centrifugal force of an absolute value F :

$$F = \omega^2 b, \text{ with } b := \Delta m r.$$

The projection of this force onto the x- and y- axis yields

$$\begin{aligned} F_x &= \omega^2 b \sin(\omega t + \phi) = \Im(\omega^2 b e^{i\phi} e^{i\omega t}), \\ F_y &= \omega^2 b \cos(\omega t + \phi) = \Re(\omega^2 b e^{i\phi} e^{i\omega t}), \end{aligned}$$

where $\Im$ and $\Re$ denote the imaginary and real part of a complex number. Those forces only apply to the displacement DOF in x-direction, and y-direction. All the other DOF are not affected. Therefore, the sub-vector $\mathbf{p}_k$ of $\mathbf{p}$ containing the entries for the DOF of the k-th node, $k =, \cdots, N$, has the form

$$\mathbf{p}_k = \begin{pmatrix} \Im(\omega^2 b_k e^{i\phi_k} e^{i\omega t}) \\ \Re(\omega^2 b_k e^{i\phi_k} e^{i\omega t}) \\ 0 \\ 0 \\ 0 \\ 0 \end{pmatrix}$$

We split $\mathbf{p}_{unb}(t) = (\mathbf{p}_k)_k$ into part with sin and cos entries only in order to apply the right hand side ansatz for each of the parts to solve (15.1):

$$\begin{aligned} \mathbf{p}_{unb} &= \Im(\mathbf{q}^1 e^{i\omega t}) + \Re(\mathbf{q}^2 e^{i\omega t}), \text{ with } \mathbf{q}^{1,2} = (\mathbf{q}_k^{1,2})_k \\ \mathbf{q}_k^1 &= \left(\Im(\omega^2 b_k e^{i\phi_k} e^{i\omega t}), 0, 0, 0, 0, 0\right)^\top \\ \mathbf{q}_k^2 &= \left(0, \Re(\omega^2 b_k e^{i\phi_k} e^{i\omega t}), 0, 0, 0, 0\right)^\top. \end{aligned} \tag{15.4}$$

Inserting the equation $\mathbf{u}_{unb}^j(t) = \mathbf{u}^j e^{i\omega t}, j = 1, 2$ and its second derivative in (15.1) yields

$$\begin{aligned} \mathbf{u}_{unb} &= \mathbf{u}_{unb}^1(t) + \mathbf{u}_{unb}^2(t), \\ &= \Im((-\omega^2 \mathbf{M} + \mathbf{S})^{-1} \mathbf{q}_1 e^{i\omega t}) + \Re((-\omega^2 \mathbf{M} + \mathbf{S})^{-1} \mathbf{q}_2 e^{i\omega t}). \end{aligned} \tag{15.5}$$

The solution of (15.1) is the sum of the particular solution $\mathbf{u}_{unb}$ and the general solution of the homogeneous equation with right hand side zero. After a certain time of rotation with a constant angular velocity and no other forces than those from unbalances the homogeneous solution will die out due to small damping effects. Hence, in this case we have the solution $\mathbf{u}_{unb}$.

15.4.2 The Process Model

The submodel for the machining process consists of two parts: a force model to simulate the actual cutting force and a model for the actual process parameters as well as the tool tip position on the workpiece surface. Actual parameter means that the parameter is time dependent in contrast to the given constant input parameters at the test stand. Figure 15.10 shows a schematic diagram of the considered diamond face turning process. In face turning the tool is moving along the x-axis with a feed velocity v_f and cuts the workpiece with a depth of cut a_p at its front face. The acting force can be split in three components, the cutting force F_c in negative y-direction, the thrust force F_t in z-direction and the feed force F_f in negative x-direction. In the considered process, the cutting velocity $v_c(t) = 2\pi n(r - d(t))$ is decreasing with time since the rotational speed n is constant but the travelled distance d is increasing. Therefore, we need a force model that includes the cutting velocity v_c in addition to the depth of cut a_p and the feed rate f defined as the distance the diamond tool is travelling during one revolution.

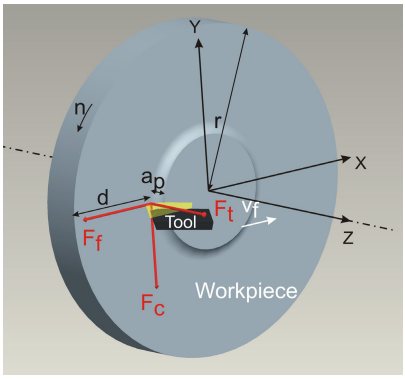

Fig. 15.10 Scheme of the considered face turning process

15.4.2.1 The Force Model

As there are a lot of standard force models for conventional cutting processes, the development of force models for micro cutting is an actual research topic, because several so called size effects occur like cutting edge effect, minimum chip thickness and ploughing effects. See [15] for an overview about size effects in cutting operations. New force models have been developed, like the recently proposed slip-line force model for micro turning with edge tool [9] including strain and temperature effects. The critical chip thickness and micro ploughing effects are also examinated, see for example [12].

In ultra-precision turning the situation is exceptional. The cutting parameters like depth of cut and feed rate are in the range of some micrometers, which is possible due to the use of diamond tools with much sharper cutting edges than conventional (carbide) tools and the application of ultraprecise machine tools. Therefore, some of the mentioned size effects do play only a subordinate role in diamond cutting

and the mentioned conventional models are not applicable to ultra-precision turning experiments. Nevertheless, the forces in the experiments show a typical behavior for micro machining and the used workpiece material (aluminium alloy AlMg3), i.e. the thrust force is the dominant force component and the forces are in the range of one Newton or less.

Another class of force models for micro turning are modified Kienzle models, see [14]. In [10] an ansatz is presented to calculate an undeformed chip thickness h which permits to consider tools with different tool nose geometries. Another modified Kienzle ansatz is proposed in [17] where the specific cutting force k_c is represented as a product of functions including cutting velocity v_c, friction μ, uncut chip thickness h and cutting edge radius r_β, i.e.

$$k_c = f_1(h) f_2(v_c) f_3(r_\beta) f_4(\mu), \tag{15.6}$$

with functions $f_1(h) = ch^{-m}$ and $f_2 = \alpha_1 v_c^{\beta_1} + \alpha_2 v_c^{-\beta_2}$. We picked up this idea and the form of the functions f_1 and f_2 to model the specific cutting force as product of functions g_i depending on the depth of cut a_p, the feed rate f and the cutting velocity v_c , i.e. to model the specific force in the form

$$k_c = g_1(a_p) g_2(f) g_3(v_c)\,. \tag{15.7}$$

Similar equations hold for the specific thrust and feed forces k_p and k_f. The functions g_i $(i = 1,2,3)$ and the model constants therein are determined with help of force measurements with different cutting conditions, see Table 15.1 for details.

Table 15.1 Experimental conditions for diamond turning experiments

Parameter	value range
rotional spindle speed	$n = 800 \ldots 1500$ rev/min
feed rate	$f = 4 \ldots 12$ mm/min
depth of cut	$a_p = 2 \ldots 14\ \mu m$
tool nose radius	$r_\varepsilon = 760\ \mu m$
workpiece material	AlMg3

The measurements of the specific forces over the depth of cut and feed rate are illustrated in Fig. 15.11 forces together with the fitted curves g_1 and g_2 (solid line) which had been determined to be of the form

$$g_1^i(a_p) = c_a^i a_p^{-m_a^i} \qquad (i = t,f,c) \tag{15.8}$$

and

$$g_2^i(f) = c_f^i f^{-m_f^i} \qquad (i = t,f,c)\,. \tag{15.9}$$

The function g_3 has been determined to be of form of the function f_2, i.e.

$$g_3^i(v_c) = \alpha_1^i v_c^{\beta_1^i} + \alpha_2^i v_c^{-\beta_2^i} \qquad (i = t,f,c)\,. \tag{15.10}$$

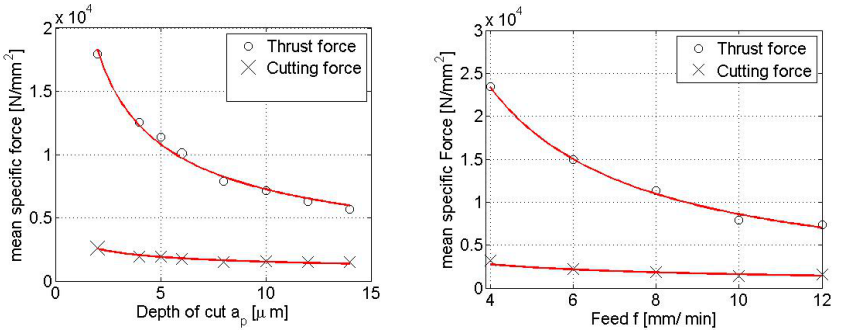

Fig. 15.11 Measured specific forces over depth of cut (left hand side) and feed (right hand side). The measured thrust force is represented by circles and the measured cutting force by x-marks. The fitted curves g_1 and g_2 given by equation (15.8) and (15.9) are plotted as solid line [3]

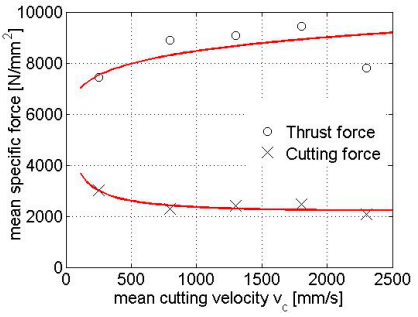

Fig. 15.12 Measured specific forces over cutting velocity. The measured thrust force is represented by circles and the measured cutting force by x-marks. The fitted curve g_3 given by equation (15.10) is plotted as solid line [3]

The function g_3 and the measurements of the specific forces over cutting velocity are shown in Fig. 15.12. Using the specific cutting forces we are now able to calculate the specific cutting force components via the usual relationship for the forces by Kienzle (see [14]):

$$F_c = k_c A_c, \qquad F_t = k_t A_c, \quad F_f = k_f A_c\,, \tag{15.11}$$

where A_c denotes the cross sectional area of cut which can be approximated by $A_c = a_p f$.

15.4.2.2 Simulation of the Tool Path

The second part of the process model consists of the simulation of the actual process parameter and the tool path. Basically, the description of the tool tip position on the surface is given by the movement of the tool, the deflections δ_i $(i = x, y, z)$ of the tool as well as the deflections Δ_i $(i = x, y, z)$ and tilting β_i $(i = x, y, z)$ of the workpiece, i.e.

$$x(t) = \quad -r + v_f t \quad -\delta_x(t) - \Delta_x(t)\,, \tag{15.12}$$

$$y(t) = \quad -\delta_y(t) - \Delta_y(t)\,, \tag{15.13}$$

$$z(t) = -a_p + \tfrac{1}{2l_h}\left(\delta_x^2 + \delta_y^2\right) + \delta_z(t) - \Delta_z(t) - x(t)\tan\left(\beta_y(t)\right)\,, \tag{15.14}$$

where l_h denotes the length of the tool holder. The angle β_y denotes the rotation of the workpiece around the y-axis. This tilt of the workpiece can influence the actual depth of the cut a_p which is described in equation (15.14). Since the deflections affect the actual tool tip position and we now define time dependent process parameters, namely the actual depth of cut

$$a_p(t) = -z(t) \tag{15.15}$$

and

$$v_x(t) = \dot{d}(t)\,, \quad \text{with } d(t) = x(t) + r\,. \tag{15.16}$$

The actual feed rate f is given by $f(t) = n^{-1} v_x(t)$. In contrast to the given constant input parameters of the test stand, the time dependant parameters are called "actual parameters".

These actual process parameters are plugged into the equation (15.11) for the force components using the equations for the specific forces (15.7). Using the actual forces, we are now able to determine the deflections of the tool holder which are proportional to the forces

$$\delta_x(t) = \frac{F_f(t)}{k_{ex}}\,, \quad \delta_y(t) = \frac{F_c(t)}{k_{ey}}\,, \quad \delta_z(t) = \frac{F_t(t)}{k_{ez}}\,. \tag{15.17}$$

Here k_{ei} denotes the corresponding stiffness in the direction i $(i = x,y,z)$. Since all force components have the same structure we get for all three spatial directions $(j = x,y,z)$ the deflection

$$\delta_j(t) = k_{ei}^{-1}\left(c_a^i\, a_p(t)^{-m_a^i}\right)\left(\tilde{c}_f^i\, f(t)^{-m_f^i}\right)\left(\alpha_1^i v_c(t)^{\beta_1^i} + \alpha_2^i v_c(t)^{-\beta_2^i}\right) a_p(t) f(t) \tag{15.18}$$

with $(i = f,c,t)$ for $(j = x,y,z)$. Derivatives of the equations for the position (15.12)-(15.14) and deflections (15.18) combined with equation (15.11),(15.15) and (15.16) for the actual parameters deliver a system of ordinary differential equations of the form

$$\dot{\delta}_x(t) = v_f - v_x(t) - \dot{\Delta}_x(t)\,, \tag{15.19}$$

$$\dot{\delta}_y(t) = \frac{1}{nk_{ey}}\left(\dot{k}_c(t) a_p(t) v_x(t) + k_c(t)\left[\dot{a}_p(t) v_x(t) + a_p(t)\dot{v}_x(t)\right]\right)\,, \tag{15.20}$$

$$\dot{\delta}_z(t) = \frac{1}{nk_{ez}}\left(\dot{k}_t(t) a_p(t) v_x(t) + k_t(t)\left[\dot{a}_p(t) v_x(t) + a_p(t)\dot{v}_x(t)\right]\right)\,, \tag{15.21}$$

$$\dot{v}_x(t) = \frac{\dot{\delta}_x(t) - n^{-1}k_{ex}^{-1} v_x(t)\left(\dot{k}_f(t) a_p(t) - k_f(t)\,\dot{a}_p(t)\right)}{n^{-1}k_{ex}^{-1} k_f(t) a_p(t)}\,, \tag{15.22}$$

$$\dot{a}_p(t) = -\frac{1}{l_h}\left(\delta_x(t)\dot{\delta}_x(t) + \delta_y(t)\dot{\delta}_y(t)\right) - \dot{\delta}_z(t) + \dot{\Delta}_x(t)\,,$$
$$+ (r - d(t))\,\frac{\dot{\beta}_y(t)}{\cos^2(\beta_y(t))} - v_x(t)\tan(\beta_y(t))\,, \tag{15.23}$$

$$\dot{d}(t) = v_x(t)\,, \tag{15.24}$$

$$\dot{k}_f(t) = -c_a^f \tilde{c}_f^f \left[a_p(t)^{-m_a^f} v_x(t)^{-m_f^f}\left(\alpha_1^f \beta_1^f v_c(t)^{\beta_1^f - 1} - \alpha_2^f \beta_2^f v_c(t)^{-\beta_2^f - 1}\right)\right.$$
$$+ \left(m_a^f a_p(t)^{-m_a^f - 1}\dot{a}_p(t) v_x(t)^{-m_f^f} + m_f^f v_x(t)^{-m_f^f - 1}\dot{v}_x(t) a_p(t)^{-m_a^f}\right)$$
$$\left.\left(\alpha_1^f v_c(t)^{\beta_1^f} + \alpha_2^f v_c(t)^{-\beta_2^f}\right)\right] \tag{15.25}$$

$$\dot{k}_c(t) = -c_a^c \tilde{c}_f^c \left[a_p(t)^{-m_a^c} v_x(t)^{-m_f^c}\left(\alpha_1^c \beta_1^c v_c(t)^{\beta_1^c - 1} - \alpha_2^c \beta_2^c v_c(t)^{-\beta_2^c - 1}\right)\right.$$
$$+ \left(m_a^c a_p(t)^{-m_a^c - 1}\dot{a}_p(t) v_x(t)^{-m_f^c} + m_f^c v_x(t)^{-m_f^c - 1}\dot{v}_x(t) a_p(t)^{-m_a^c}\right)$$
$$\left.\left(\alpha_1^c v_c(t)^{\beta_1^c} + \alpha_2^c v_c(t)^{-\beta_2^c}\right)\right]\,, \tag{15.26}$$

$$\dot{k}_t(t) = -c_a^t \tilde{c}_f^t \left[a_p(t)^{-m_a^t} v_x(t)^{-m_f^t}\left(\alpha_1^t \beta_1^t v_c(t)^{\beta_1^t - 1} - \alpha_2^t \beta_2^t v_c(t)^{-\beta_2^t - 1}\right)\right.$$
$$\left(m_a^t a_p(t)^{-m_a^t - 1}\dot{a}_p(t) v_x(t)^{-m_f^t} + m_f^t v_x(t)^{-m_f^t - 1}\dot{v}_x(t) a_p(t)^{-m_a^t}\right)$$
$$\left.\left(\alpha_1^t v_c(t)^{\beta_1^t} + \alpha_2^t v_c(t)^{-\beta_2^t}\right)\right]\,. \tag{15.27}$$

Hereby, we defined $\tilde{c}_f^i = c_f^i n^{m_f^i}$, because of the relation $v_x(t) = nf(t)$ and equation (15.9). The cutting velocity is calculated by $v_c(t) = 2\pi n\,(r - d(t))$ and the vibrations Δ_i, $i \in \{x, y, z\}$, as well as the tilt angle β_y of the workpiece and their derivatives are determined by the structural submodel. The system of differential equations will be solved numerically with the MATLAB solver "ode15i". The stiffness values k_{ei} $(i = x, y, z)$ are determined by the geometrical dimensions of the tool holder and its elasticity module (material: steel, $E = 210$ kN/mm^2). The resulting actual forces F_i are calculated by the deflections δ using equation (15.17). The numerical results are presented in Sect. 15.4.5.

15.4.3 Coupling of the Submodels

In the last two sections both submodels have been presented, the structure model and the process model. Solving the ODE (15.1) lead to the vibrations u of all elements of the discretization. The first six entries are related to the workpiece and are input parameters for the system of differential equations (15.19)-(15.27), i.e.

$$(\Delta_x, \Delta_y, \Delta_z) = (u_1, u_2, u_3) \qquad \text{and}\, \beta_y = u_5\,. \tag{15.28}$$

The process model computes the actual forces and deflections of the tool which act at the tool tip position on the workpiece. Therefore, these forces add up to the forces

of the unbalances in the right hand side of equation (15.1). The resulting additional load vector has the form

$$\mathbf{p}_{cut}(t,\mathbf{u}(t)) = (F_f, F_c, F_t, 0, M_c, M_t, 0, \cdots, 0)^T, \qquad \text{with } M_{\{t,c\}} = F_{\{t,c\}} \times r_a,$$

where $r_a(t) = r - d(t)$ denotes the radius of the workpiece minus the already travelled distance of the tool on the workpiece, cf. Fig. 15.10. Thus, a coupled system of ODEs

$$\begin{aligned} \mathbf{M}\ddot{\mathbf{u}}(t) + \mathbf{S}\mathbf{u}(t) &= \mathbf{p}_{unb} + \mathbf{p}_{cut}\left(t, \mathbf{F}(t,\mathbf{w}), M_t(t,\mathbf{w}), M_c(t,\mathbf{w})\right), \\ \dot{\mathbf{w}}(t) &= g\left(t, \mathbf{w}(t), \dot{\mathbf{w}}(t), \mathbf{u}(t)\right), \end{aligned}$$

has to be solved, where the function g is given by the system of differential equations (15.19)-(15.27) and the corresponding variables are collected in the vector $\mathbf{w} = (\delta_x, \delta_y, \delta_z, v_y, a_p, d, k_t, k_f, k_c)$. In order to solve the non-linear coupled system approximately, we have employed a time step algorithm and assumed the forces and moments from the cutting process to be constant during a small time interval, i.e. $\mathbf{p}_{cut}(t) = \mathbf{p}_{cut}(t_i)$ for $t \in [t_i, t_i + \Delta t]$. Now,

$$\mathbf{u}(t) = A(\mathbf{p}_{unb} + \mathbf{p}_{cut}(t_i)), \quad t \in [t_i, t_i + \Delta t],$$

where A describes the solution operator of (15.1). The resulting deflections $(\Delta_x, \Delta_y, \Delta_z)$ from (15.28) are plugged into the force model and we compute

$$(F_f(t_{i+1}), F_c(t_{i+1}), F_t(t_{i+1})) = B(\mathbf{u}(t_i + \Delta t)) = B(\delta_x, \delta_y, \delta_z)$$

at $t_{i+1} = t_i + \Delta t$. Here B denotes the solution operator for solving (15.19)-(15.27) and use (15.17) afterwards. Again, we assume the cutting forces to be constant over the next time interval $[t_{i+1}, t_{i+1} + \Delta t]$. This routine is repeated until the end of the desired time interval $t \in [t_0, t_{end}]$ is reached, for which the coupled system should be solved.

15.4.4 Surface Visualization

The visualization of a three-dimensional representation of a surface is an intuitive but powerful and flexible technique in surface characterization and comparison. Surfaces produced in face turning can be represented as a continuous function $S(x,y)$ describing the surface height over the (x,y)-plane. For visualization and other digital processing, (x,y) is an element of a discrete support set consisting of regular or irregular arranged points. For objective characterization, three dimensional surface parameters can be derived from the surface function S, see [16] for more details.

We make investigations to study the surface at two scales. We are interested in the form deviation of the global workpiece but also in the roughness structure. During the development it turns out to be more efficient to decompose large surfaces into two scales and to simulate both scales separately. This is done not only for the save of computation time but also for avoiding alias effects which may occur when

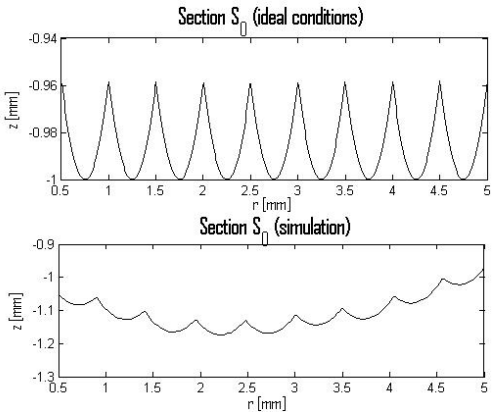

Fig. 15.13 Radial surface sections under ideal conditions and for a simulation, both with $a_p = 1\text{mm}$, $f = 0.5\text{mm}$, $r_\varepsilon = 0.76\text{mm}$

large surfaces at fine discretization are sampled down. Consequently, we calculate S on a small rectangular sub domain at fine discretization to visualize the roughness profile and to determine the local surface parameters. Therefore, a kinematic surface simulation is developed in the following subsections. The global form is provided by S, evaluated on selected tool tip positions.

15.4.4.1 Simulation of Surface Generation

The ideal kinematic surface resulting from face turning can be described by a set of radial sections. Each radial section S_k is built by repetitions of the edge geometry in intervals of feed per revolution. If a round nosed tool of radius r_ε is used, we can formulate each radial section by

$$S_k(x) = r_\varepsilon - \sqrt{r_\varepsilon^2 - \left(x + (k - 1/2)f - \left\lfloor \frac{x + kf}{f} \right\rfloor f\right)^2} - a_p, \quad x \in [0, r], k \in [0, 1),$$

where $k2\pi$ denotes the section's angle. An ideal radial section S_0 is shown in Fig. 15.13. The surface profile will change in two ways with respect to vibrations of the workpiece and deflections of the tool. Firstly, the repetitions will not be necessarily equidistant and the turning grooves will differ in their depth. Secondly, the geometry of each channel will change because tool and workpiece will not be positioned orthogonal to each other. Figure 15.13 shows also a simulation result for a disturbed process.

In the following, a discrete surface generation model, which is coupled with the process model, is presented to provide the surface function S depending on vibrations of the workpiece and tool deflection. The central component of the model is the parameter to state operator

$$\Phi : P \to \mathbb{R}^{4\times 4}, \tag{15.29}$$

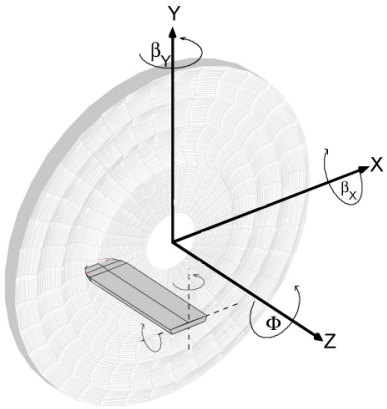

Fig. 15.14 Coordinate system for dynamic surface simulation; rotational motion of workpiece and tool

which maps kinematic information, provided by the structure model, to homogeneous matrices used to formulate the tool trajectories.

15.4.4.2 Calculation of the Tool Trajectories

Basically, the interacting objects, workpiece and tool, are assumed to be solid such that they are configured in the coordinate system for any time point t by a rotation and a translation. Thus, the tool and workpiece trajectories are given by affine linear mappings Φ_T and Φ_W. In computer graphics homogeneous matrices are used to perform such transformations. Therefore, we introduce a homogeneous coordinate system, which is built from cartesian coordinates by

$$(x,y,z) \mapsto (x,y,z,1). \tag{15.30}$$

The characteristic motions in turning processes are the rotation of the workpiece around the z-axis, which is expressed by

$$\Phi_W = R_Z(\phi) = \begin{pmatrix} \cos(\phi) & -\sin(\phi) & 0 & 0 \\ \sin(\phi) & \cos(\phi) & 0 & 0 \\ 0 & 0 & 1 & 0 \\ 0 & 0 & 0 & 1 \end{pmatrix},$$

and the translation of the tool along the x-axis, which is expressed by

$$\Phi_T = T((r - fNt, 0, l_h - a_p)) = \begin{pmatrix} 1 & 0 & 0 & r - fNt \\ 0 & 1 & 0 & 0 \\ 0 & 0 & 1 & l_h - a_p \\ 0 & 0 & 0 & 1 \end{pmatrix}.$$

These two operators describe the movement of the tool and of the workpiece under ideal conditions. The positioning and alignment errors are included into the model by applying further translations and rotations. Figure 15.14 shows the tilt angles β_x

and β_y of the workpiece. The moment acting around the x-axis has only a marginal effect to surface generation, and therefore it is neglected in our model. The rotation rate is assumed to be constant. This leads to the operator for the movement of the workpiece:

$$\Phi_W = T(\Delta)R_Y(\beta_y)R_Z(\phi). \tag{15.31}$$

The tool inclination is changed appropriate to the deflection provided by the force model by applying multiple rotations, which leads to

$$\Phi_T = T((r - fNt, 0, l_h - a_p))R(\delta_x, \delta_y).$$

So far, the movement of the tool is described by Φ_T and that one of the workpiece by Φ_W. For the material removal algorithm the relative position of the tool to the workpiece is compulsory. Φ_W and Φ_T give absolute positions, but we can carry over the workpiece operation to the tool using

$$\Phi := \Phi_W^{-1}\Phi_T. \tag{15.32}$$

The diamond tool, or more precisely its edge geometry, can be parameterized as

$$\varepsilon(\varphi) = (r_\varepsilon \cos\varphi, 0, -r_\varepsilon \sin\varphi - l + r_\varepsilon, 1)^T, \quad \varphi \in [0, \pi], \tag{15.33}$$

with tool radius r_ε and length l_h. Thus, the relative tool trajectories are given by $\Phi\varepsilon(\varphi)$ for $\varphi \in [0, \pi]$. In case of ideal conditions, i.e. no vibration, no displacement and no deflection, (15.32) can be written as

$$\Phi = \begin{pmatrix} \cos(-\phi) & -\sin(-\phi) & 0 & (r - fNt)\cos(-\phi) \\ \sin(-\phi) & \cos(-\phi) & 0 & (r - fNt)\sin(-\phi) \\ 0 & 0 & 1 & l_h - a_p \\ 0 & 0 & 0 & 1 \end{pmatrix}. \tag{15.34}$$

In Fig. 15.15 the ideal and disturbed tool tip locus is visualized. For the ideal case the trajectories of the tool tip are given by applying the tool tip $\varepsilon(\pi/2) = (0, 0, -l, 1)^T$ to (15.34), leading to $(x, y, z, 1)^T = ((r - fNt)\cos(-\phi), (r - fNt)\sin(-\phi), -a_p, 1)^T$, i.e. a spiral with decreasing radius appropriate to the feed rate located parallel to the workpiece surface at height $-a_p$.

15.4.4.3 Material Removal Process

The material removal takes place under ideal conditions, i.e. a homogeneous, isotropic material and an ideal sharp tool in the sense of a cutting edge $r_\beta = 0$ are assumed. Consequently, the material passed by the cutting edge will be removed completely, in particular no ploughing or elastic recovery is considered. Therefore, the swept volume of the moving edge

$$\Phi\varepsilon(\varphi_i), \quad 0 = \varphi_0 < \cdots < \varphi_n = \pi$$

is used to update the surface function S for points, which are passed by the cutting edge.

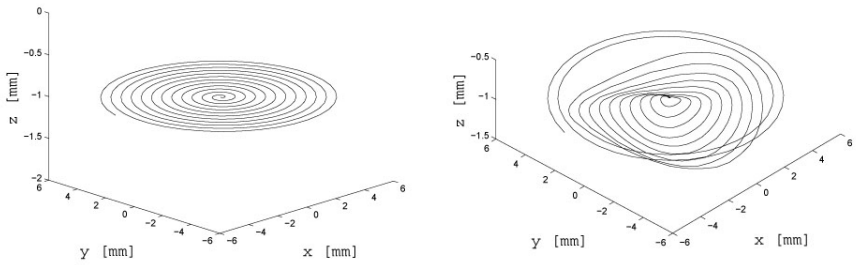

Fig. 15.15 Relative tool tip locus for ideal conditions (left) and for an oscillating surface (right); $a_p = 1$mm, f=0.5mm

15.4.5 Numerical Simulation Results

Following Sections 15.4.4.2 and 15.4.4.3, a surface generation model for micro turning processes has been implemented. The model is able to simulate the global form and roughness structure of the machined surface depending on the balancing state of the machine. As mentioned in 15.4.2, the differential equations system for the process model is solved numerically. The ODE (15.1) of the structure model is solved numerically, too. A detailed description how to reformulate and solve the problem is proposed in [2]. All algorithms are implemented in the mathematical programming environment MATLAB. First, we tested the algorithm with different time steps Δt. The experiments showed that for higher frequencies the time resolution has be chosen smaller. In particular, for the rotational speeds in our simulation we have to use time steps equal or less than 1 ms.

We then tested the algorithm for several parameter settings. As expected, the presence of unbalances mainly affects the deflection or vibration amplitudes in radial direction x and y. Nevertheless, the deflection in z direction is affected, too. We can also observe quantitative effects for unbalance distributions of different magnitude. Here, we will only present one example with the parameters defined in Table 15.2, setting 1. We have used two different sets of unbalance distributions $\mathbf{f}_1 = ([22.4\ gmm, 63°], [4.5\ gmm, 243°], [4.7\ gmm, 2°])$ and $\mathbf{f}_2 = ([22.4\ gmm, 63°]$, $[0.45\ gmm, 243°]$, $[0.47\ gmm, 2°])$. The first position corresponds to the workpiece, the second and the third to the balancer planes.

Figure 15.16 shows the development of the deflection of the workpiece in direction of the spindle over time for both unbalance settings. The vibration in radial direction as well as the development of the depth of cut are shown in Fig. 15.17. Fig. 15.18 presents the thrust force F_t and the cutting force F_c. The higher unbalance distribution $\mathbf{f}_1$ causes vibrations with bigger amplitudes.

Table 15.2 Parameter setting for the simulations

Parameter	setting 1	setting 2	setting 3
rotational spindle speed	$n = 25\,\text{Hz}$	$n = 25\,\text{Hz}$	$n = 20\,\text{Hz}$
feed rate	$f = 5.33\ \mu\text{m/rev}$	$f = 500\ \mu\text{m/rev}$	$f = 8.33\ \mu\text{m/rev}$
depth of cut	$a_p = 5\ \mu\text{m}$	$a_p = 5\ \mu\text{m}$	$a_p = 5$
tool nose radius	$r_\varepsilon = 760\ \mu\text{m}$	$r_\varepsilon = 760\ \mu\text{m}$	$r_\varepsilon = 760\ \mu\text{m}$
workpiece radius	$r = 30$ mm	$r = 5$ mm	$r = 30$ mm
tool holder length	$l_h = 25$ mm	$l_h = 25$ mm	$l_h = 25$ mm
time step	$\Delta t = 1$ ms	$\Delta t = 0.1$ ms	$\Delta t = 1$ ms

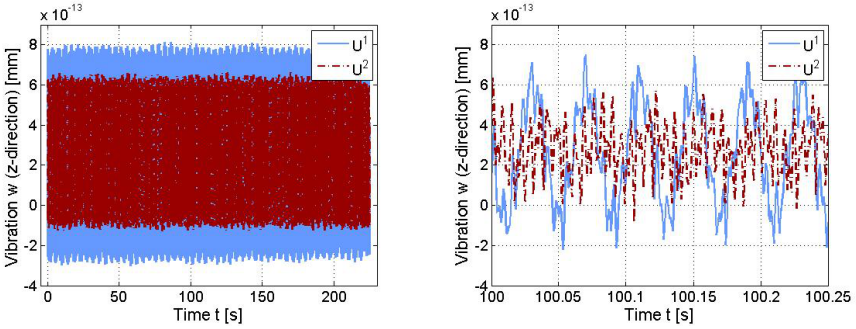

Fig. 15.16 Deflection of the workpiece in z-direction for $\mathbf{f}_1$ and $\mathbf{f}_2$; entire time interval (left), and detail (right)

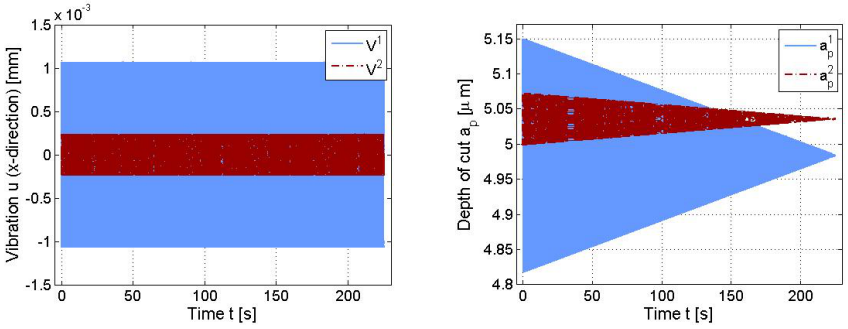

Fig. 15.17 Deflection of the workpiece in y-direction for $\mathbf{f}_1$ and $\mathbf{f}_2$ and depth of cut

The output of the process machine interaction model can also used to visualize the machined surface. In a first step, surface simulations for simple oscillations of type

$$\beta_y(t) = \sum_i k_i \sin(p_i \omega t), \quad \omega = n2\pi, \tag{15.35}$$

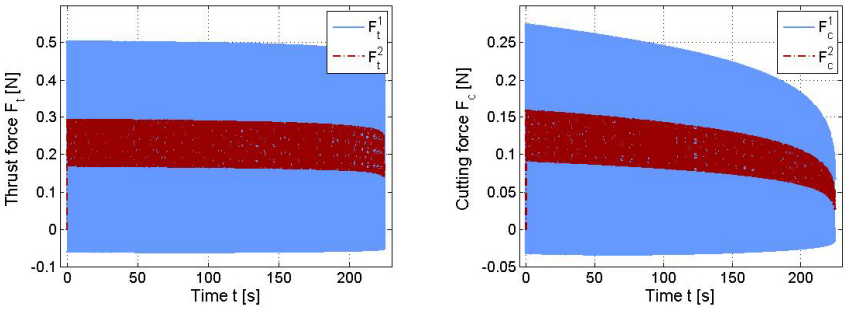

Fig. 15.18 Simulated thrust and cutting force

are carried out in order to verify the basic function of the surface model. It is clear that frequencies $p_i n$ in the signal β_y can be recovered in the surface structure because the workpiece is rotating with angular speed ω. In Fig. 15.19 two example surfaces for different oscillations are shown.

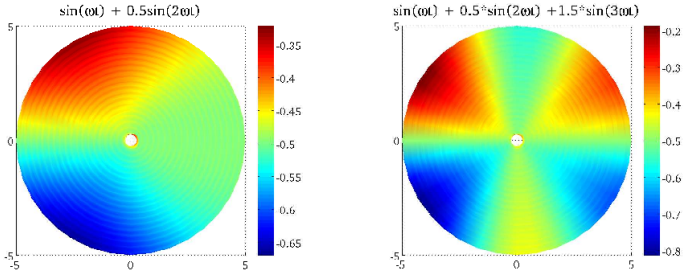

Fig. 15.19 Simulated surfaces for oscillations of type (15.35)

In a second step, the robustness of surface generation is evaluated with the help of the implemented surface model. This is an important step, because all input oscillations are result of numerical solved differential equations. Figure 15.20 shows exemplarily a simulated surface for an oscillation β_y of $(50+\varepsilon)$Hz, where ε denotes a small disturbance. When no disturbance exists ($\varepsilon = 0$) and a rotation frequency of 50Hz is assumed, the resulting surface is an inclined plane. With increasing degree of disturbance the form error grows rapidly, which is demonstrated in Figure 15.20 for $\varepsilon = 10^{-4}, 10^{-3}, 10^{-2}$. For $\varepsilon = 10^{-4}$ a first distortion appears, which is growing intensively for increasing disturbance. Finally, for $\varepsilon = 10^{-2}$ the oscillation is heavily asynchronous to the rotation leading to a completely wrong visual impression.

Model problems with reduced workpiece diameter and high feed speeds are considered for the benefit of short calculation time for all sub-models. The process parameters of setting 2 in Table 15.2 are used in three model problems with different unbalance configurations, see Table 15.3. The related surfaces are plotted in

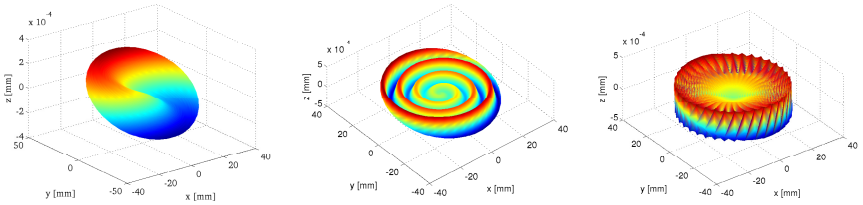

(a) $\varepsilon = 10^{-4}$ (b) $\varepsilon = 10^{-3}$ (c) $\varepsilon = 10^{-2}$

Fig. 15.20 Simulated surfaces for an oscillation of $(50+\varepsilon)$Hz; $n = 50$Hz, $r = 30$mm

Fig. 15.21 (a)–(c). In case (a), where no unbalances are set, a wavy surface can be detected. This corresponds to the power spectrum of β_y, where three different frequencies can be identified. In case (b) and (c), where unbalances for the workpiece or balancer planes are set, only the rotation frequency can be identified in the power spectrum. The result is an inclined surface.

Table 15.3 Unbalance configuration for the model problems of setting 2

no.	unbalance workpiece	unbalance balancer planes 1 and 2
(a)	no	no
(b)	no	$([4.5\ gmm, 243°], [4.7\ gmm, 2°])$
(c)	$[22.4\ gmm, 63°]$	$([4.5\ gmm, 243°], [4.7\ gmm, 2°])$

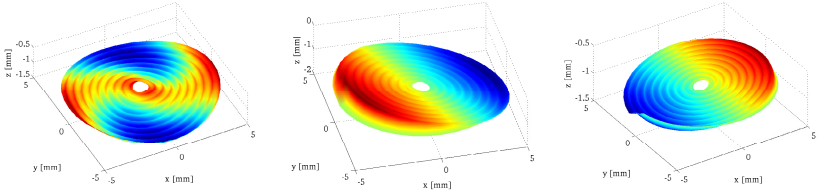

(a) No Unbalances (b) Plane 1&2 set (c) Unbalance at workpiece and plane 1&2 set

Fig. 15.21 Simulated surfaces for model problems

In a last step, surfaces under practical relevant conditions concerning workpiece dimension and process parameters are computed. For a workpiece diameter of 60 mm and a feed rate of $5.33\mu m$ more than 5.600 overlapping channels generate the resulting surface. To realize simulation results with reasonable expense, a two scale model is compulsory. In analogy to the experiments, a set of simulations for different rotation rates ($n = 1200, \ldots, 1800\ [\text{min}^{-1}]$) and feed rates ($f = 5.33, \ldots, 8.33\ [\mu\text{m}]$) with two different balancing states are carried out. In the unbalanced case, only the

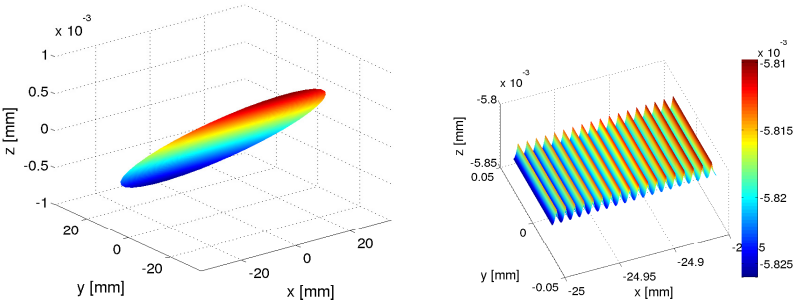

(a) Global form (b) Roughness profile

Fig. 15.22 Simulated surfaces for setting 3, Table 15.2, unbalanced (1.823g at the workpiece)

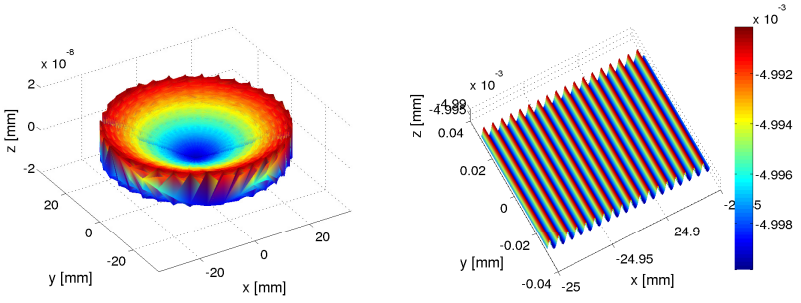

(a) Global form (b) Roughness profile

Fig. 15.23 Simulated surfaces for setting 3, Table 15.2, best possible balancing state

rotation frequency can be identified in the oscillations $\beta_x, \beta_y, \beta_z$. The displacements and deflections are relatively small compared to the dominant oscillation β_y and the resulting surface is an inclined plane. The global form and a small rectangular domain of $150\mu\text{m} \times 50\mu\text{m}$ are plotted in Figure 15.22. In the case of best possible balancing state, β_y indicates one frequency, which is close to the rotation frequency, e.g. 48.96Hz for $n = 50$Hz. It can be assumed that this deviation is of numerical nature. The simulated surface is highly defective, see Figure 15.23, and corresponds to the scenario shown in Figure 15.20 (c).

15.5 Solving the Inverse Problem for Balancing

So far, we presented a process-machine interaction model which can compute the surface topography of the workpiece with a given unbalance distribution and input process parameters. Mathematically spoken, we have derived an operator A which

maps the vector p containing the unbalances distribution and the process parameters to a surface S, i.e. we have the following operator equation

$$\mathbf{A}(p) = S. \tag{15.36}$$

This equation is called forward formulation of our model. Assuming now that for a given surface S, we are interested do determine the necessary balancing state in order to obtain the surface S, i.e. to solve equation (15.36) with respect to p. However, measurement devices typically have limited precision and we assume that unprecise and noisy measurement data S_δ are available, which fulfill $||S - S_\delta|| \leq \delta$, where δ denotes the measurement precision. Usually this operator is not continuously invertible, which means that for given noisy data S_δ with a data error of the function $p^\delta = \mathbf{A}^{-1}(S_\delta)$ might be an arbitrary bad approximation of the true unbalance distribution p. Problems with those properties are referred to as being ill-posed. In this case, least square techniques, where p^δ is computed as the minimizer of $\|\mathbf{A}p - S_\delta\|^2$, are unstable. The computation of p^δ can be stabilized by using the regularization methods presented in Chap. 3, i.e. by minimizing the so-called Tikhonov-functional

$$p_\alpha^\delta = \min_p \|\mathbf{A}p - S_\delta\|_2 + \alpha\Psi(p) \tag{15.37}$$

instead. The penalty term $\Psi(p)$ acts as a stabilizer and prevents large values of $\Psi(p)$.Typical choices of Ψ are, e.g.

$$\Psi(p) = \|p\|_p := \left(\sum_i |p_i|^p\right)^{1/p}, 0 < p \leq 2. \tag{15.38}$$

In a first attempt we invert the structural submodel, i.e. given a vibration u we determine the unbalance distribution p causing the vibrations. This results are presented in Chap. 3. Future work is dealing with the inversion of the full forward problem (15.36).

15.6 Experimental Results

Face turning experiments were conducted to show to which extent an unbalance affects the resulting surface topography. To further assist the investigation and understanding of the process-machine-interaction force measurements were carried out during machining.

There are two main effects which result from an unbalance. First, the spindle on which the unbalance is acting is deflected and performs a tumbling motion which leads to a differing tool path. Second, the unbalance induces a vibration to the whole machine tool structure where the magnitude of this vibration depends on the damping properties of the machine tool. These effects have different influences with regard to the process, surface topography and process forces.

15.6.1 Form Deviation

The initial experiments showed a trend to higher form deviations (peak to valley, s. Fig. 15.24) for unbalanced workpieces or workpieces which were machined with an additional unbalance. In this context unbalanced workpiece means a workpiece without any balancing procedures prior to machining. An additional unbalance is a weight added to the workpiece by the use of setscrews to amplify balance induced effects.

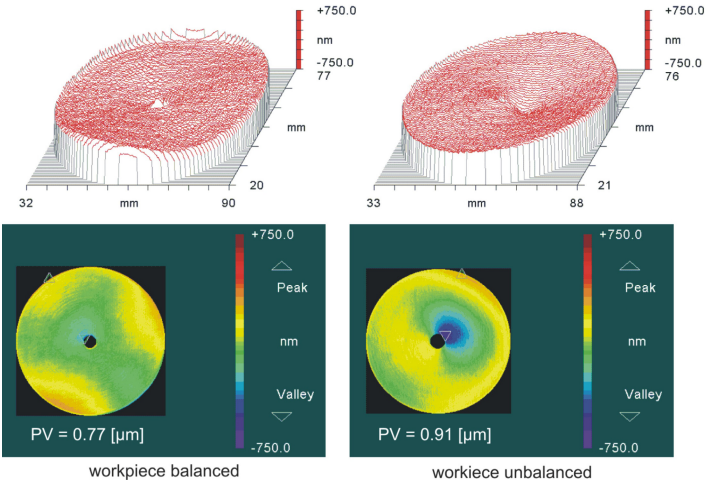

Fig. 15.24 Form deviations for balanced (left) and unbalanced (right) workpiece [11]

The influence of an unbalance in terms of form deviation can be seen in Fig. 15.25 and Fig. 15.26. The diagrams show the form deviation versus the depth of cut and feed. Additionally, the cross sectional area of cut A_c is given for each experiment series. In correspondence to previous experiments workpieces with unbalance show a larger form deviation in general. Larger cross sectional areas of cut show similar form deviations for workpieces with and without unbalances compared to smaller cross sectional areas of cut. It is assumed that the engagement of the tool is damping the unbalance induced vibration and the tumbling motion of the workpiece respectively and therefore leads to similar values of form deviation compared to machined workpieces without unbalance.

15.6.2 Surface Roughness

The initial experiments could not show a clear dependency between unbalance and surface roughness as large deviations within the roughness data prevented any clear correlation [5]. Additionally, the roughness values are still within the limit of 10 nm *Ra* (i.e. optic quality) in the majority of the cases for machining with unbalance.

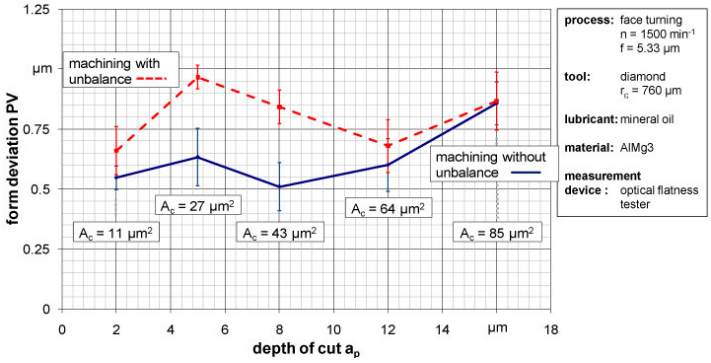

Fig. 15.25 Form deviation vs. depth of cut (with and without unbalance) [11]

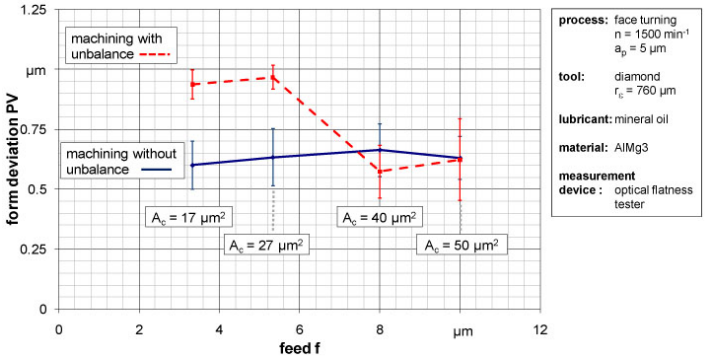

Fig. 15.26 Form deviation vs. feed (with and without unbalance) [11]

From Fig. 15.27 and Fig. 15.28 it can be seen that the difference between machining with and without unbalance are only marginal. The roughness values are slightly higher for machining with unbalance but for the observed cutting parameters no strong influence can be observed.

Possibly the test stand is working at its limit in terms of accuracy as it has a lower stiffness compared to current ultraprecision machine tools. Another possibility for the low influence of unbalances is assumed in the process kinematic, as for turning the surface normal and the direction of the force generated by the un-balance are perpendicular to each other. For that reason the workpiece will not be deflected directly in direction of the tool which would cause a periodical change for the depth of cut. Therefore, the current investigations will be extended by ultraprecision milling experiments. For these experiments the normal of the generated surface and the direction of the unbalance induced forces and with that the motion of the tool will be the same.

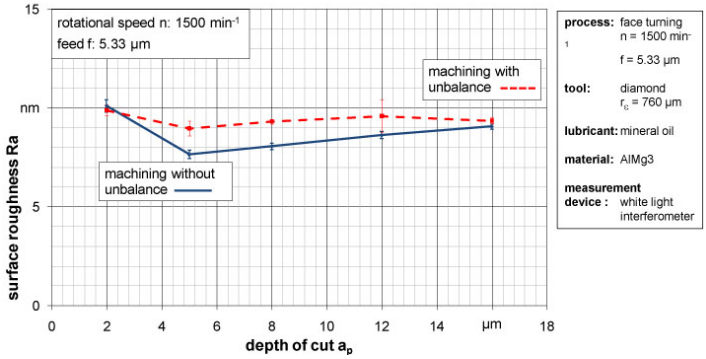

Fig. 15.27 Surface roughness vs. depth of cut (with and without unbalance) [11]

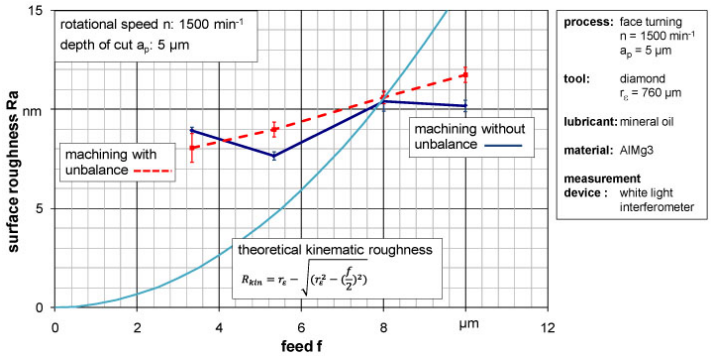

Fig. 15.28 Surface roughness vs. feed (with and without unbalance)

15.6.3 Force Measurements

For the used workpiece material (AlMg3) the measured forces showed a characteristic order in terms of their magnitude. The influencing effect of the unbalance is always largest for the thrust force, followed by the cutting force and the feed force with the lowest values.

Figure 15.29 shows the components of the resulting forces versus the depth of cut. The dashed line represents the experiments where an unbalance was applied, the continuous line represents the experiments in balanced state.

As expected, the forces rise with an increase for the depth of cut. From these experiments it can be seen that there is a significant difference between balanced and unbalanced workpieces only for the thrust force, whereas the cutting force and the feed force are almost equivalent for balanced and unbalanced states. As the thrust force is depending on the friction of the chip on the rake face, it is estimated that the thrust force will have a specific value for a balanced workpiece. In addition, if the workpiece is unbalanced, it will be deflected and perform a tumbling

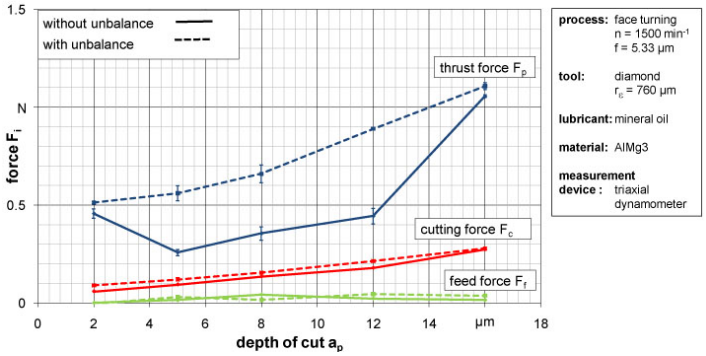

Fig. 15.29 Process forces F_i vs. depth of cut [11]

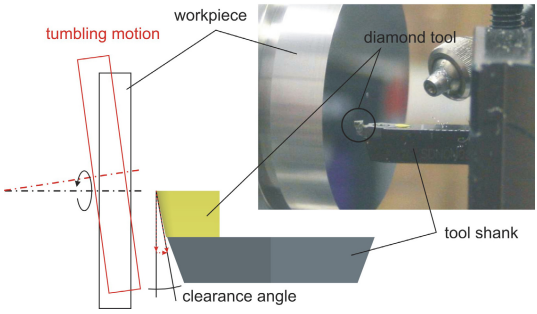

Fig. 15.30 Changed clearance angle because of tumbling motion [11]

motion additionally to the rotation. The tumbling motion will tilt the workpiece periodically with respect to the tool. The tilting will not change the friction between chip and rake face, but the angle between the workpiece surface and clearance face will change periodically. For balanced machining this angle will be equivalent to the clearance angle. For unbalanced machining if the workpiece is tilting towards the clearance face, this angle will decrease and induce a larger frictional load on the clearance face. With this additional frictional load the increased thrust force for unbalanced workpieces can be explained. The cutting force would have been expected to show a significant rise for unbalanced machining, because of the change in the depth of cut. But at this stage this phenomenon cannot be explained.

A similar behavior for the force components can be recognized for an increasing feed, again only the thrust force is influenced by the unbalance (see [11]).

15.7 Summary and Outlook

Up to now only single plane balancing has been used for ultraprecision machining processes although a secondary balancing plane seems promising with regard

to an optimized surface quality. Utilizing a test stand with dual-plane-balancing capabilities machining experiments have been conducted to show the dependence between balancing quality and surface generation.

Additionally, a modelling approach of the interaction between machining process and machine tool structure has been developed. Two submodels (structure model and process model) are combined in a nonlinear way, and the resulting interaction model is solved numerically by a time step algorithm. The solution is used as a basis to determine the surface topography and the surface quality by using a surface simulation program which is still under development. The setup of the mathematical model is supported by the experimental data.

The mathematical model of the dependency between unbalances and surface topography will enable us to predict the surface quality of a workpiece for a given balancing state of the machine as well as to compute the balancing state which is necessary at least for a given surface quality. Additionally, the necessary balancing weights can be determined efficiently from vibrational measurements at the casing of the machine. This will reduce time to setup the machine for the cutting process with a desired accuracy.

The experimental investigations showed an influence of the balancing quality with respect to the form deviation of the machined workpieces. The form deviation rose for machining with an additional unbalance. But for the same parameters the form deviation decreased if the cross sectional area of cut was increased, which was accounted for with a higher damping of the engaged tool. Although it was assumed for unbalanced machining to have an impact on surface roughness, machining with an additional unbalance showed only marginal differences compared to balanced machining. Due to its adjustment possibilities the test stand is not as stiff as standard ultraprecison machine tools, we assume that the lower stiffness is responsible for difficulties in showing a clear dependency between unbalance and surface roughness.

Surprisingly only the thrust force was considerably affected by the unbalances. Cutting force and feed force did not show any clear effects for unbalanced machining. This behavior has not been anticipated, least for the cutting force. The lack of influence with respect to the cutting force cannot be explained at this stage.

As the project is still in progress it is planned to investigate circumferential milling as an additional ultraprecision machining process. For this process the direction of the unbalance induced centrifugal force and the direction of the surface normal are the same. Therefore, any motion of the tool in radial direction will directly affect the surface generation. Consequently the influence of unbalances on the surface topography will be larger than for turning.

Acknowledgements. The presented research has been funded by the German Research Foundation DFG within the Priority Program 1180.

References

1. DIN ISO 1940-1 mechanical vibration - balance quality requirements for rotors in a constant (rigid) state - part 1: Specification and verification of balance tolerances
2. Brandt, C., Niebsch, J., Ramlau, R., Maass, P.: Modeling the influence of unbalances for ultra-precision cutting processes. ZAMM - Journal of Applied Mathematics and Mechanics/Zeitschrift für Angewandte Mathematik und Mechanik 91(10), 795–808 (2011), doi:10.1002/zamm.201000155
3. Brandt, C., Niebsch, J., Vehmeyer, J.: Modelling of ultra-precision turning process in consideration of unbalances. In: 13th CIRP Conference on Modeling of Machining Operations (2011)
4. Brinksmeier, E., Gläbe, R., Krause, A.: Precision balancing in ultraprecision diamond machining. In: Laser Metrology and Machine Performance 8, Lamdamap 2007, vol. 8, pp. 262–269 (2007)
5. Brinksmeier, E., Krause, A.: Dual plane balancing for diamond machining processes. In: 3rd International Conference High Performance Cutting (HPC), Dublin, pp. 517–528 (2008)
6. Brinksmeier, E., Krause, A.: Surface generation in ultraprecision diamond machining utilising dual-plane-balancing. In: International Conference on Process Machine Interactions, Hannover, pp. 335–342 (2008)
7. Brinksmeier, E., Riemer, O.: Deterministic prodcution of complex optical elements. International Journal of Production Engineering and Computers - Special Issue on CAPP and Advances in Cutting Technology 4(5), 63–72 (2002)
8. Gasch, R., Knothe, K.: Strukturdynamik Bd. 2: Kontinua und ihre Diskretisierung. Springer, Berlin (1989); IX, 336 S: graph. Darst
9. Jin, X., Altintas, Y.: Slip-line field model of micro-cutting process with round tool edge effect. Journal of Materials Processing Technology (2010) (in press), doi:10.1016/j.jmatprotec.2010.10.006
10. Köhler, J.: Berechnung der Zerspankräfte bei variierenden Spanungsquerschnittsformen. Ph.D. thesis, Leibniz Universität Hannover (2010)
11. Krause, B.: Process forces in diamond machining with consideration of unbalances. In: CIRP PMI, Vancouver (2010)
12. Malekian, M., Park, S., Jun, M.: Investigation of critical chip thickness and micro ploughing forces. In: Proceedings of the 2nd International Conference on Process Machine Interactions, Vancouver, Canada, June 10-11 (2010)
13. Schneider, H.: Auswuchttechnik. Springer (2007)
14. Tönshoff, H.K., Denkena, B.: Spanen: Grundlagen, 2., erw. und neu bearb. aufl edn. Springer, Berlin (2004); XXIV, 417 S.: Ill., graph. Darst
15. Vollertsen, F., Biermann, D., Hansen, H., Jawahir, I., Kuzman, K.: Size effects in manufacturing of metallic components. CIRP Annals - Manufacturing Technology 58(2), 566–587 (2009), doi:10.1016/j.cirp.2009.09.002
16. Dong, W.P., Blunt, L.: Three-dimensional surface topography, 2nd edn. Penton Press (2000), `http://www.sciencedirect.com/science/book/9781857180268`, XXII, 285 S
17. Weber, M., Autenrieth, H., Kotschenreuther, J., Gumbsch, P., Schulze, V., Lohe, D., Fleischer, J.: Influence of friction and process parameters on the specific cutting force and surface characteristics in micro cutting. Machining Science and Technology 12, 474–497 (2008), doi:10.1080/10910340802518728
18. Zhou, S., Shi, J.: Active balancing and vibration control of rotating machinery: A survey. The Shock and Vibration Digest 33, 361–371 (2001)